CAMBRIDGE
UNIVERSITY PRESS

Research Article

A new radio continuum study of the large magellanic cloud supernova remnant MC SNR J0519–6902

Rami Z. E. Alsaberi[1,2], Miroslav D. Filipović[2], Hidetoshi Sano[1,3,4], Shi Dai[2], Frank Haberl[5], Patrick J. Kavanagh[6], Denis Leahy[7], Pierre Maggi[8], Gavin Rowell[9], Manami Sasaki[10], Ivo R. Seitenzahl[11], Dejan Urošević[12,13], Jeffrey Payne[2], Zachary J. Smeaton[2], and Sanja Lazarević[2,14,15]

[1]Faculty of Engineering, Gifu University, 1-1 Yanagido, Gifu 501-1193, Japan, [2]Western Sydney University, Locked Bag 1797, Penrith NSW 2751, Australia, [3]Center for Space Research and Utilization Promotion (c-SRUP), Gifu University, 1-1 Yanagido, Gifu 501-1193, Japan, [4]National Astronomical Observatory of Japan, Mitaka, Tokyo 181-8588, Japan, [5]Max-Planck-Institut für extraterrestrische Physik, Gießenbachstraße 1, D-85748 Garching, Germany, [6]Department of Physics, Maynooth University, Maynooth, Co Kildare, Ireland, [7]Department of Physics and Astronomy, University of Calgary, University of Calgary, Calgary, Alberta, T2N 1N4, Canada, [8]Observatoire Astronomique de Strasbourg, Université de Strasbourg, CNRS, 11 rue de l'Université, F-67000 Strasbourg, France, [9]School of Physical Sciences, The University of Adelaide, Adelaide 5005, Australia, [10]Remeis Observatory and ECAP, Universität Erlangen-Nürnberg, Sternwartstraße 7, D-96049 Bamberg, Germany, [11]Heidelberg Institute for Theoretical Studies (HITS), Schloss-Wolfsbrunnen Weg 35, 69118, Heidelberg, Germany, [12]Department of Astronomy, Faculty of Mathematics, University of Belgrade, Studentski trg 16, 11000 Belgrade, Serbia, [13]Isaac Newton Institute of Chile, Yugoslavia Branch, [14]CSIRO Space and Astronomy, Australia Telescope National Facility, PO Box 76, Epping, NSW 1710, Australia and [15]Astronomical Observatory, Volgina 7, 11060 Belgrade, Serbia

Abstract

We present a new radio continuum study of the Large Magellanic Cloud supernova remnant (SNR) MC SNR J0519–6902. With a diameter of ∼8 pc, this SNR shows a radio ring-like morphology with three bright regions towards the north, east, and south. Its linear polarisation is prominent with average values of $5 \pm 1\%$ and $6 \pm 1\%$ at 5 500 and 9 000 MHz, and we find a spectral index of -0.62 ± 0.02, typical of a young SNR. The average rotation measure is estimated at -124 ± 83 rad m^{-2} and the magnetic field strength at ~ 11 μG. We also estimate an equipartition magnetic field of 72 ± 5 μG and minimum explosion energy of $E_{min} = 2.6 \times 10^{48}$ erg. Finally, we identified an H I cloud that may be associated with MC SNR J0519–6902, located in the southeastern part of the remnant, along with a potential wind-bubble cavity.

1. Introduction

Supernova remnants (SNRs) play an essential role in the structure of galaxies, enriching the Interstellar Medium (ISM) as well as having a significant impact on the structure and physical properties of the ISM. The study of SNRs in our own Galaxy is not ideal because of difficulties of making accurate distance measurements. Instead, we study SNRs in nearby, small, dwarf galaxies, including the Large Magellanic Cloud (LMC) located at a distance of 50 kpc (Macri et al., 2006; Pietrzyński et al., 2019). Because all objects within this galaxy are located at approximately the same distance, physical measurements, including the physical size, are more reliable. The almost face-on orientation of the LMC (inclination angle of ∼35°, van der Marel & Cioni, 2001) allows deep, high-resolution (spatial and spectral) multi-frequency observations (Maggi et al., 2016; Bozzetto et al., 2017). Moreover, the LMC contains active star-forming regions, and is located away

from the Galactic plane where absorption by gas and dust is reasonably low.

To date, numerous studies have investigated SNRs within the LMC. Maggi et al. (2016) reported 59 SNRs as X-ray emitters, and the radio-continuum studies of Bozzetto et al. (2017) have added 15 candidates to that list. Leahy (2017) studied the most energetic and brightest LMC SNRs using an analysis of the Maggi et al. (2016) SNR sample. Maitra et al. (2019, 2021) promoted two additional objects as bona fide SNRs; Yew et al. (2021) discovered two new optical SNRs and 14 candidates. Most recently, Kavanagh et al. (2022); Bozzetto et al. (2023); Filipović et al. (2022); Zangrandi et al. (2024) confirmed eight new LMC SNRs and suggested an additional 15 as 'good' candidates. This currently gives us a total of 71 confirmed LMC SNRs and an additional 20 candidates. Thirteen SNRs are confirmed and two candidates are possible Type Ia remnants (Bozzetto et al., 2017).

MC SNR J0519–6902 (also known as LHG 26) was initially discovered using the *Einstein* observatory (Long et al., 1981). Tuohy et al. (1982) confirmed the SNR is Balmer-dominated with a broad Hα component. They reported an X-ray angular size of ∼30" and an optical angular size of 28" with a forward shock velocity of $2\,900 \pm 400$ km s^{-1}. They suggest the remnant is expanding

into a low-density region composed of neutral hydrogen, inferring a Type Ia Type Ia Supernova (SN) with an estimated progenitor mass of between 1.2 and 4.0 $M_\odot$. Kosenko et al. (2010) used *Chandra* and *XMM-Newton* observations to estimate the velocity for the forward shock of $2\,770 \pm 500$ km s^{-1} with no strong non-thermal X-ray continuum emission. Hovey et al. (2018) used optical data to report a forward shock velocity of 2 650 km s^{-1}.

Chu & Kennicutt (1988) associated MC SNR J0519–6902 with the nearby (200 pc) population II OB association – LH41. Desai et al. (2010) found no young stellar object associated with this SNR, while Edwards et al. (2012) reported that this SNR could have only been a Type Ia SN event resulting from a supersoft X-ray source or a double degenerate system.

Mathewson et al. (1983) estimated a radio spectral index [a] for MC SNR J0519–6902 of $\alpha=-0.6$, while Mills et al. (1984) reported an index of –0.65. Bozzetto et al. (2012) listed a spectral index of -0.53 ± 0.07, which still suggested predominantly synchrotron emission (e.g. Filipović & Tothill, 2021) from a typical young SNR (Reynolds et al., 2012; Galvin & Filipovic, 2014; Bozzetto et al., 2017; Maggi et al., 2019).

Tuohy et al. (1982) inferred an age for MC SNR J0519–6902 of $\sim$500 yrs while Smith et al. (1991) reported an age between 500 and 1 500 yrs. Rest et al. (2005) used a light echo method to estimate an age of 600 ± 200 yrs. Based on *Chandra* and *XMM-Newton* observations, Kosenko et al. (2010) suggested an age of 450 ± 200 yrs. Leahy (2017) used X-ray emission and temperature to derive an age of $\sim$2 700 yrs, assuming a shock radius of 4.1 pc expanding in a uniform ISM.

Dickel & Milne (1995) observed this remnant with the Australia Telescope Compact Array (ATCA) at 1 472 and 2 368 MHz. They estimated an average fractional polarisation across the remnant of $1.5 \pm 0.6\%$ and $4.1 \pm 0.6\%$, respectively. Bozzetto et al. (2012), who estimated the diameter of this SNR at $\sim$8 pc, found average fractional polarisation values of $\sim$2.2% and $\sim$3.2% at 5 500 and 9 000 MHz, respectively. They also calculated a calculated a rotation measure (*RM*) for the entire remnant of $\sim$10 rad m^{-2}.

Vukotic et al. (2007) estimated the magnetic field of this SNR, using both a classic and revised equipartition formula to obtain results of 186 and 270 μG, respectively. Bozzetto et al. (2012) used the modified equipartition model from Arbutina et al. (2012) to estimate the magnetic field to be $\sim$171 μG with a minimum energy of $E_{min} = 1.8 \times 10^{49}$ erg.

Kosenko et al. (2015) reported a method based on state-of-the-art 3D simulations of thermonuclear SN explosions, coupled with hydrodynamic calculations of SNR evolution, while making use of the most up-to-date atomic data to suggest MC SNR J0519–6902 originated from an oxygen-rich merger. Seitenzahl et al. (2019) discovered optical ([Fe XIV] 5303 Å) emission associated with this SNR. Li et al. (2019) searched for a surviving companion of MC SNR J0519–6902 and found a candidate run-away companion star moving at a radial velocity of 182 km s^{-1}.

In this paper, we present new high-resolution ATCA radio continuum images of MC SNR J0519–6902 at 5 500 and 9 000 MHz. In Section 2 we describe our observations and data analyses. Our new findings and discussion are listed in Section 3. Finally, our conclusions are outlined in Section 4.

[a] This is defined by $S_\nu \propto \nu^\alpha$, where S_ν is flux density, ν is frequency, and α is the spectral index.

Table 1. ATCA observations of MC SNR J0519–6902.

Date	Project Code	Array Config.	Int. Time on source (minutes)	References
15th Nov 2011	C634	EW367	$\sim$30	Bozzetto et al. (2012)
01st Jan 2015	CX310	6A	$\sim$50	This work
28th Dec 2019	CX454	1.5C	$\sim$500	This work

2. Observation and data analysis

2.1 Radio continuum observations

We observed MC SNR J0519–6902 with ATCA (project codes: CX454 and CX310). ATCA archival[b] data (project code: C634) were also used to produce the high-resolution and sensitive images (see Table 1). All observations were carried out in "snap-shot" mode, with 1-hour of integration over a 12-hour minimum using the Compact Array Broadband Backend (CABB) (2048 MHz bandwidth) at wavelengths of 3/6 cm ($\nu = 4\,500$–$6\,500$ and $8\,000$–$10\,000$ MHz centred at 5 500 and 9 000 MHz) totalling $\sim$580 minutes integration. The primary (flux density) calibrator, PKS B1934–638, with a flux density of 4.96 Jy for 5 500 MHz and 2.70 Jy for 9 000 MHz, and the secondary (phase) calibrator, PKS B0530–727, with a flux density of 0.77 Jy for 5 500 MHz and 0.82 Jy for 9 000 MHz were used for all three observing days.

MIRIAD[c] (Sault et al., 1995) and KARMA[d] (Gooch, 1995) software packages were used for data reduction and analysis. Imaging was completed using the multi-frequency synthesis INVERT task with natural Briggs weighting (robust = 0 for both 5 500 and 9 000 MHz). Beam sizes included $2.3'' \times 1.7''$ and $1.4'' \times 1.0''$ for 5 500 and 9 000 MHz images, respectively. MFCLEAN and RESTOR algorithms allowed the images to be deconvolved, with primary beam correction applied using LINMOS. We followed the same process for stokes Q and U images using a smoothed resolution of $5'' \times 5''$ (see Section 3.2).

2.2 H I observations

Archival H I data (Kim et al., 2003) were obtained using the ATCA and Parkes 64-m telescope. The angular resolution of the data is $60''$, corresponding to a spatial resolution of $\sim$15 pc at the distance of the LMC. The typical noise level is $\sim$2.4 K at a velocity resolution of 1.689 km s^{-1}.

2.3 Chandra observations

We used archival X-ray data obtained using *Chandra* for which the observation IDs (Obs IDs) are 118 (PI: S. Holt), 11 241, 12 062, and 12 063 (PI: J. P. Hughes); the data have been published by several authors (e.g., Kosenko et al., 2010; Edwards et al., 2012; Schenck et al., 2016). All datasets were taken using the Advanced CCD Imaging Spectrometer S-array (ACIS-S3) in June 2000 (Obs ID 118), December 2009 (Obs IDs 11241 and 12062), and in February 2010 (Obs ID 12063). We utilised Chandra Interactive Analysis

[b] Australia Telescope Online Archive (ATOA), hosted by the Telescope National Facility (ATNF): https://atoa.atnf.csiro.au
[c] http://www.atnf.csiro.au/computing/software/miriad/
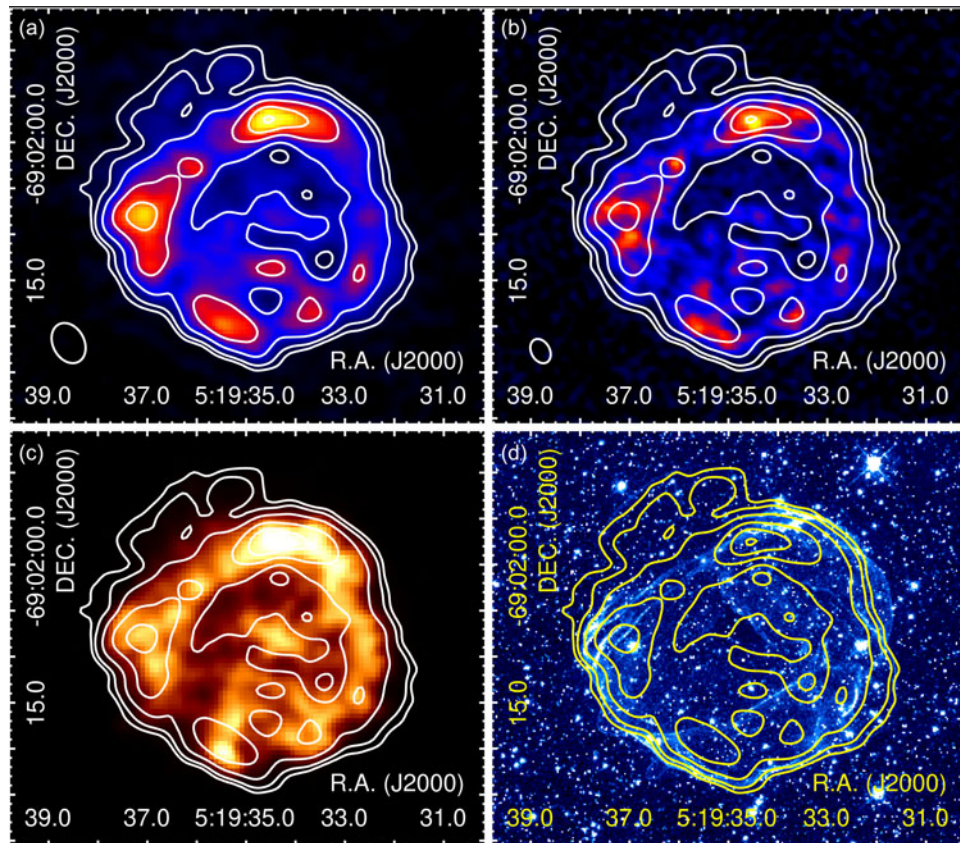[d] http://www.atnf.csiro.au/computing/software/karma/

Figure 1. *(a)* ATCA image at 5 500 MHz of MC SNR J0519–6902. The ellipse in the lower left corner represents a synthesised beam of 2.3″ × 1.7″ with a p.a. of 62°. *(b)* ATCA image at 9 000 MHz. The ellipse in the lower left corner represents a synthesised beam of 1.4″ × 1.0″ with a p.a. of 61°. The rms noise of the 5 500 and 9 000 MHz images is 20 μJy beam^{-1} and 17 μJy beam^{-1}, respectively. *(c) Chandra* broadband image. *(d)* HST image (combination of the V-band and Hα images, Edwards et al., 2012). 5 500 MHz contour lines overlaid on each image are 0.05, 0.09, 0.2, 0.4, 0.6, and 0.8 mJy beam^{-1}.

of Observations (CIAO, Fruscione et al., 2006) version 4.12 with CALDB 4.9.1 for data reprocessing and imaging. "Chandra_repro" and "merge_obs" scripts created an exposure-corrected, energy-filtered image at 0.5–7.0 keV (hereafter referred to as "broadband") with a total effective exposure of ∼91 ks. Lastly, we smoothed the image with a Gaussian kernel of 1″, Full Width at Half-Maximum (FWHM).

2.4 Optical HST observations

The *Hubble Space Telescope* (HST) image of MC SNR J0519–6902 was downloaded from the Mikulski Archive for Space Telescopes[e] portal. All details regarding these HST observations and their data reduction are described in Edwards et al. (2012).

3. Results and discussion

3.1 Radio morphology

MC SNR J0519–6902 has a ring-like morphology with three bright regions towards the north, east, and south (Bozzetto et al., 2012). In Figure 1, the new ATCA images at 5 500 and 9 000 MHz are compared with the *Chandra* and HST images. Root Mean Squared (rms) noise for these high resolution ATCA images at 5 500 and 9 000 MHz are ∼20 and ∼17 μJy beam^{-1}, respectively; one order of magnitude better than that obtained by Bozzetto et al. (2012).

The figure clearly shows a radio emission coincident with X-ray emission suggesting relativistic electrons are associated with the shock-heated gas. Interestingly, the optical emission is outside both the radio continuum and X-ray emission (Figure 1), indicating the optical emission is located at the forward shock. The radio morphology of this SNR is asymmetric in terms of variation in brightness. As noted by Bozzetto et al. (2012), it features three bright regions located in the north, east, and south (Figure 1), resembling the structure of LMC SNR N 103B (Alsaberi et al., 2019) and Kepler in the Milky Way (MW) (DeLaney et al., 2002). Moreover, our new images show a faint structure on the north-east side of MC SNR J0519–6902 which was not present in previous images (see Figure 1). Although not statistically significant ($< 3\sigma$), this feature suggests that the SNR extends further in the north-east direction compared to the other sides (see text for details).

We used the Minkowski tensor analysis tool BANANA[f] (Collischon et al., 2021) to determine the centre of expansion. This tool searches for filaments and calculates normal lines and line

density maps. For a perfect shell, all lines should meet at the centre position inside the SNR, where the expansion must have started (see Collischon et al., 2021, for more details). Since real sources deviate from this ideal picture, we circumvented this problem by smoothing the line density map using a circle with a diameter of 40 pixels. We then took the centre position of the pixel where the line density was the highest. Using the same method, we performed the tensor analysis separately for the 5 500 MHz, 9 000 MHz, and *Chandra* broad-band images. From this, we calculated the mean centre position and the 1σ uncertainty of the mean.

The resulting calculated centre is RA (J2000) $= 05^h19^m34.85^s$, Dec (J2000) $= -69°02'08.22''$ with an uncertainty of $\sim$0.1 arc-sec. This is $\sim$0.32'' ($\sim$0.07 pc at the distance of 50 kpc) south-west from the previous estimation by Bozzetto et al. (2012) (RA(J2000) $= 05^h19^m34.9^s$, Dec (J2000) $= -69°02'07.9''$). To calculate the radio continuum radius of this SNR, we used the MIRIAD task CGSLICE to plot 16 equispaced radial profiles in $22.5°$ segments around the remnant at 5 500 MHz. Each profile is 25'' in length (Figure 2). We divide the remnant into four equal regions: south-west (profiles 1–5), south-east (profiles 5–9), north-east (profiles 9–13), and north-west (profiles 13–1) (Figure 2a). We identify the cutoff as the point where each profile intersects the outer contour line (3σ ATCA image contour or 60 μJy beam^{-1} at 5 500 MHz). These cutoffs are represented as dashed vertical lines (see Figure 2b, c, d, and e). The thick black vertical lines represent the average of the cutoffs in each region. The resulting radii vary from $16.46 \pm 1.19''$ (3.99 ± 0.28 pc) towards the south-west (Figure 1b) to $16.08 \pm 1.14''$ towards the south-east (3.89 ± 0.27 pc; Figure 2c) and $18.44 \pm 0.75''$ (4.47 ± 0.18 pc) towards the north-east (Figure 2d) to $16.34 \pm 0.93''$ (3.96 ± 0.22 pc) towards the north-west (Figure 2e) with an average of $16.83 \pm 1.08''$ (4.08 ± 0.26 pc) for the entire SNR. This is consistent with a previous estimation by Bozzetto et al. (2012). The size of this SNR is close to SNRs of similar age, J0509–673 (Bozzetto et al., 2014) in the LMC and Kepler (Patnaude et al., 2012) in the MW.

3.2 Polarisation

The fractional polarisation for MC SNR J0519–6902 was calculated using the Equation:

$$P = \frac{\sqrt{S_Q^2 + S_U^2}}{S_I},$$ (1)

where P is the average fractional polarisation, and S_Q, S_U, and S_I are integrated intensities for the Q, U, and I stokes parameters, respectively.

MC SNR J0519–6902 fractional polarisation vectors appear prominent in 5 500 and 9 000 MHz maps (see Figure 3), we also present polarisation intensity maps in the same figure. The average fractional polarisation values are $5 \pm 1\%$ and $6 \pm 1\%$ for 5 500 and 9 000 MHz, respectively. These are fractionally lower than the values reported by Bozzetto et al. (2012) but consistent within the errors, and higher than the values of low frequencies (1 472 and 2 368 MHz) reported by Dickel & Milne (1995). They are similar to the values of N 103B of $\sim$8% at 5 500 MHz (Alsaberi et al., 2019) in the LMC, Kepler of $\sim$ 6% at 4 835 MHz (DeLaney et al., 2002), and G1.9+0.3 of 6% at 5 500 MHz (De Horta et al., 2014) in the MW.

3.3 Spectral index

The radio spectra of MC SNR J0519–6902 can be described as a pure power-law of frequency.

We used the MIRIAD (Sault et al., 1995) task IMFIT to extract a total integrated flux density from all available radio continuum observations of MC SNR J0519–6902 listed in Table 2. This includes observations from the Murchison Widefield Array (MWA) (For et al., 2018), Molonglo Observatory Synthesis Telescope (MOST) (Clarke et al., 1976; Mauch et al., 2003), Australian Square Kilometre Array Pathfinder (ASKAP) (Pennock et al., 2021), and ATCA. We measured the MWA flux density for each sub-band (76–227 MHz) and we also re-measured the ASKAP flux density at 888 MHz from Pennock et al. (2021). All arrays are sensitive to angular scales much larger than the size of the SNR. Therefore, the sampling of the *uv* plane for different arrays and at different frequencies would not affect flux density measurements of extended structures. For cross-checking and consistency, we used AEGEAN (Hancock et al., 2018) and found no significant difference in integrated flux density estimates. Namely, we measured MC SNR J0519–6902 local background noise (1σ) and carefully selected the exact area of the SNR which also excludes all obvious unrelated point sources. We then estimated the sum of all brightnesses above 5σ of each individual pixel within that area and converted it to SNR integrated flux density following (Findlay, 1966, Equation 24). We also estimate that the corresponding radio flux density errors are below 10% as examined in our previous work (Filipović et al., 2022; Bozzetto et al., 2023).

In Figure 4, we present the flux density vs. frequency graph for MC SNR J0519–6902. The relative errors are used for the error bars on a logarithmic plot. The best power-law weighted least-squares fit is shown (thick red line), with the spatially integrated spectral index $\langle \alpha \rangle = -0.62 \pm 0.02$; slightly steeper but within range when compared to Bozzetto et al. (2012). This spectral index is consistent with values of similar aged SNRs such as Kepler (–0.64, Dickel et al., 1988) and SN 1006 (–0.6, Gardner & Milne, 1965) within the MW.

We also produced a spectral index map using 5 500 and 9 000 MHz images. To create this, all images were first re-gridded to the finest pixel size ($0.26'' \times 0.26''$) using the MIRIAD task REGRID. The images were then smoothed to a common resolution ($3'' \times 3''$) using CONVOL. Finally, MATHS was applied to create the spectral index map and its corresponding error map as shown in Figure 5. The average spectral index value across the remnant was found to be -0.7 ± 0.2. We note that the uncertainty value is an order of magnitude higher than the estimate from Figure 4. This is because the error map of spectral index was generated using only two images (5 500 and 9 000 MHz).

3.4 Rotation measure and magnetic field

To calculate the *RM* of MC SNR J0519–6902, the 2 048 MHz bandwidth at 5 500 MHz was split into four 512 MHz sub-bands (4 723, 5 244, 5 756, and 6 268 MHz). Using position angle measurements associated with fractional polarisation maps for these frequencies, the MIRIAD task IMRM was applied. *RM* values with an error $\geq$ 120 rad m^{-2} were flagged. The resulting *RM* map is shown in Figure 6. We note the *RM* values are mostly negative with some positive values towards the north and west of the remnant. Values
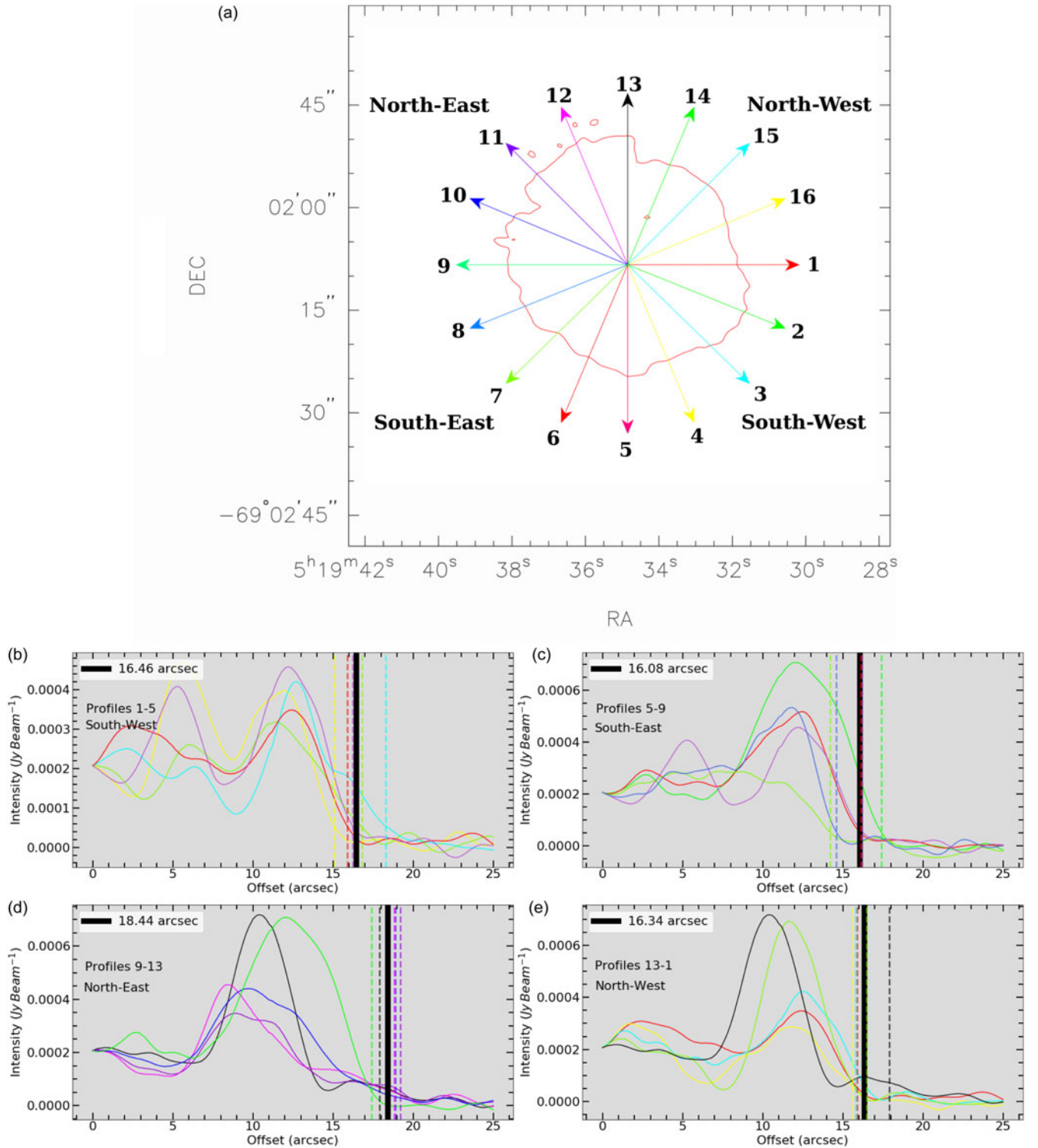
Figure 2. Estimate of the radio continuum radius of MC SNR J0519–6902 at 5 500 MHz. a: Radial profiles around the remnant from the centre (see Section 3.1) overlaid on the 3σ ATCA image contour (60 μJy beam^{-1}) at 5 500 MHz. The central position of the remnant is RA (J2000) $= 05^h19^m34.85^s$, Dec (J2000) $= -69°02'08.22"$. b, c, d, and e: Radial profiles. The dashed vertical lines represent profile cut-offs and the thick black vertical lines represent the average of the cutoffs (in arcsec) for different parts of the shell; south-west, south-east, and north-east, and north-west, respectively.
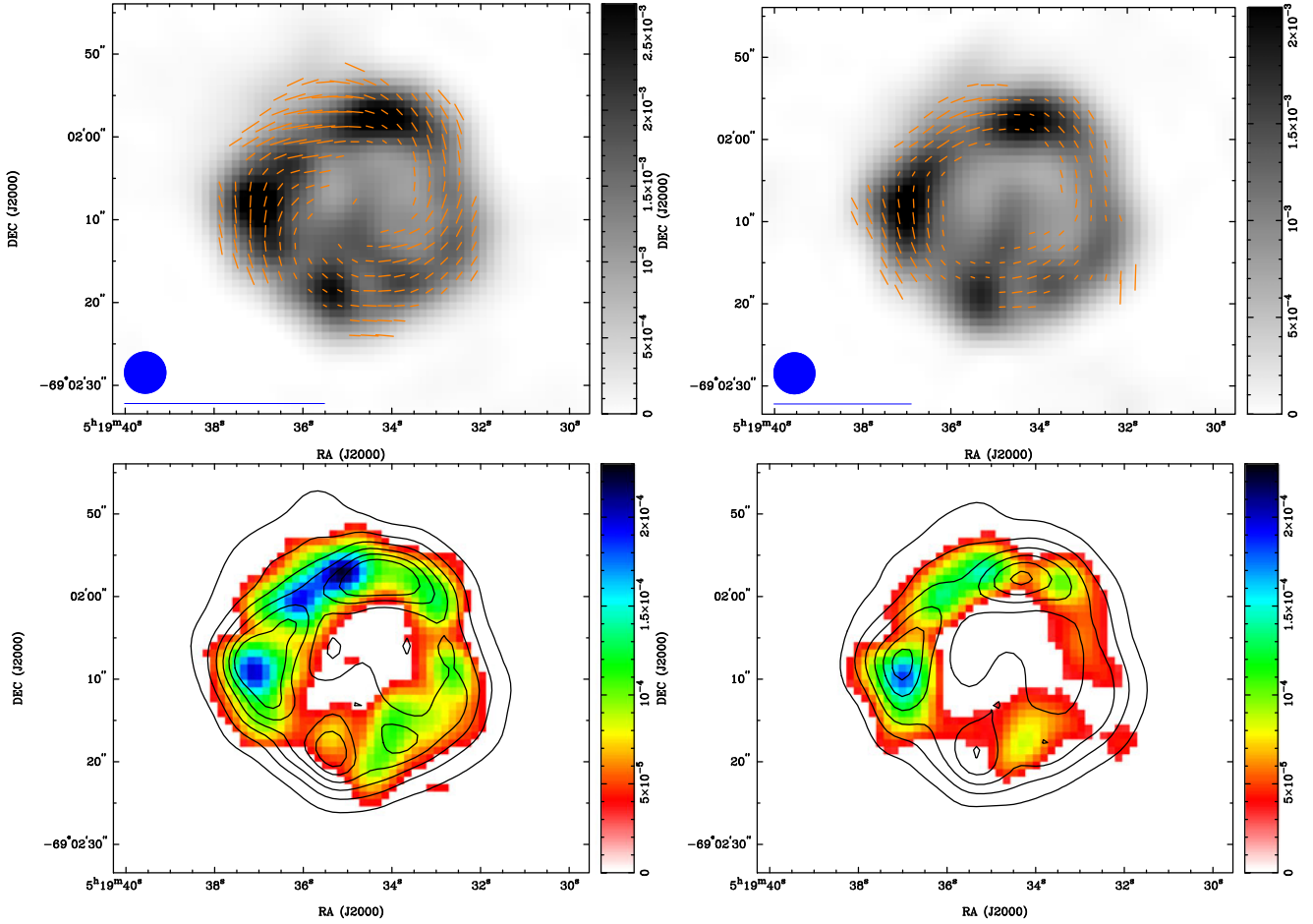
Figure 3. Fractional Polarisation vectors of MC SNR J0519–6902 overlaid on the intensity ATCA images at 5 500 MHz (upper left) and at 9 000 MHz (upper right). The blue circle in the lower left corner represent a synthesised beam of 5″ × 5″ and the blue line below the circle represents 100% polarisation. The bar on the right side represents the greyscale of the intensity images in Jy beam^{-1}. Polarisation intensity maps of MC SNR J0519–6902 at 5 500 MHz (bottom left) and at 9 000 MHz (bottom right) are shown at bottom with intensity image contour lines overlaid. Respective contour levels are 0.2, 0.6, 1, 1.4, 1.8, and 2.2 mJy beam^{-1} for both images. The colour bar represents gradients of polarisation intensity.

of *RM* are concentrated in three areas of the remnant; north-east, north, and north-west (see Figure 6), with an average value of -124 ± 83 rad m^{-2}, different than the value reported by Bozzetto et al. (2012). Once the *RM* had been determined, the vectors were rotated back to their intrinsic (zero wavelength) values. In Figure 7 an additional 90° was added to the electric vectors so that the vectors represent the direction of magnetic-fields within the remnant. These vectors are oriented in a radial direction (see Figure 7), as expected from a young SNR.

To calculate the electron density (n_e) for MC SNR J0519–6902, we used Equation 2, where *EM* is the emission measure in cm^{-3}, *D* is the distance to the SNR; n_e and n_p are electron and proton densities, respectively.

$$EM = \int n_e * n_p \, dV/(4\pi D^2), \qquad (2)$$

By assuming $n_e = 1.2 \, n_p$, a volume filling factor $= 1$, an isotropic and spherical distribution of ionised gas, and using an *EM* $\sim 22.5 \times 10^{58}$cm^{-3} (Maggi et al., 2016), we obtain $n_e = 6.8$ cm^{-3}.

The magnetic field strength can be estimated using the Equation for Faraday depth[g]:

$$RM = 811.9 \int_0^L n_e B_\parallel \, dl, \qquad (3)$$

where *RM* is the rotation measure in rad m^{-2}, n_e is the electron density in cm^{-3}, $B_\parallel$ is the line of sight magnetic field strength in μG, and *L* is the path length through the Faraday rotating medium in kpc (Clarke, 2004).

Using our average value of *RM* (–124 rad m^{-2}), an SNR thickness (*L*) of the compressed shell of ~ 2 pc, and an n_e value of 6.8 cm^{-3}, we obtain an average magnetic field strength of 11.2 μG.

The equipartition model[h] can also be used to estimate the magnetic field strength for MC SNR J0519–6902. This method uses modeling and simple parameters to estimate the intrinsic magnetic

---

[g]This assumes only one source along the line of sight with no internal Faraday rotation; the Faraday depth approximates the rotation measure of all wavelengths.

[h]Online calculator is found at http://poincare.matf.bg.ac.rs/~arbo/eqp

Table 2. Flux density measurements of MC SNR J0519–6902. The asterisk (*) indicates that we re-measured this flux density.

Freq. (MHz)	Flux Density (Jy)	Telescope	Reference
143	0.360	MWA	This work
150	0.370	MWA	This work
158	0.433	MWA	This work
166	0.391	MWA	This work
173	0.408	MWA	This work
181	0.385	MWA	This work
189	0.354	MWA	This work
196	0.350	MWA	This work
204	0.351	MWA	This work
212	0.318	MWA	This work
219	0.401	MWA	This work
227	0.405	MWA	This work
408	0.150	MOST	Bozzetto et al. (2012)
843	0.145	MOST	Bozzetto et al. (2012)
888	0.129*	ASKAP	Pennock et al. (2021)
1472	0.100	ATCA	Dickel & Milne (1995)
2368	0.070	ATCA	Dickel & Milne (1995)
4 800	0.044	ATCA	Bozzetto et al. (2017)
5 500	0.045	ATCA	This work
8 640	0.033	ATCA	Bozzetto et al. (2017)
9 000	0.033	ATCA	This work
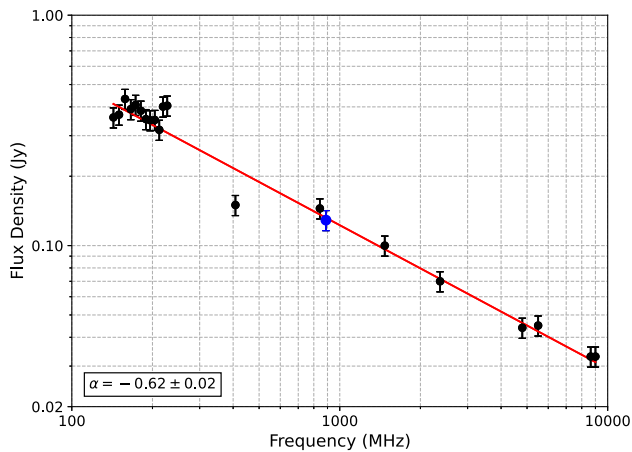
Figure 4. Radio continuum spectrum of MC SNR J0519–6902. The blue dot indicates that we re-measured this flux density.

field strength and energy contained in the magnetic field and cosmic ray (CR) particles using radio synchrotron emission (Arbutina et al., 2012; Arbutina et al., 2013; Urošević et al., 2018).

This approach is purely analytical, described as a rough, only order of magnitude estimate because of assumptions used in analytical derivations and errors in the determination of distance, angular diameter, spectral index, a filling factor, and flux density, tailored especially for the magnetic field strength in SNRs. Arbutina et al. (2012); Arbutina et al. (2013); Urošević et al. (2018) present two models; the difference is in the assumption whether

there is equipartition, precisely constant partition with CRs or only CR electrons. Urošević et al. (2018) showed the latter type of equipartition is a better assumption than the former.

Using the Urošević et al. (2018) model[i], the mean equipartition field over the entire remnant is $72 \pm 5\ \mu G$ with an estimated minimum energy of $E_{min} = 2.6 \times 10^{48}$ erg. However, using the Arbutina et al. (2012) earlier model, which assumes CRs composed of electrons, protons, and ions, the estimate is $156 \pm 5\ \mu G$, with a minimum explosion energy of $E_{min} = 1.2 \times 10^{49}$ erg. This is consistent with previous values reported by Bozzetto et al. (2012).

Of course, we cannot suppose we know the remnant's magnetic field to the significant figures implied above as the models do not have any such accuracy. We do feel it is reasonable to say MC SNR J0519–6902's magnetic field can be estimated between 10 and 10^2 μG. This is consistent with other relatively young Type Ia SNRs including Tycho, Kepler, and SN 1006 (Reynolds & Ellison, 1992).

3.5 Σ–D relation

A previous Σ–D diagram (Urošević 2022; Urošević, 2020; Pavlović et al., 2018, their Figure 3) was compared with our values, D∼8 pc and $\Sigma_{1\,GHz} = 6 \times 10^{-20}$ W m^{-2} Hz^{-1} sr^{-1}, for MC SNR J0519–6902. This comparison implies the MC SNR J0519–6902 is undergoing expansion within a surrounding environment characterised by a low-density of 0.005–0.02 cm^{-3} with an initial energy of explosion of $E_0 = 10^{51}$ erg (Figure 8). MC SNR J0519–6902 position at Σ–D tracks can set it somewhere at the end of the free expansion phase, close to entering the early Sedov phase of evolution.

Of course, multiple tracks can correspond to a single SNR on the Σ–D plane. Assuming this is a young SNR, it is unlikely that the black and red lines would apply. If the evolutionary tracks are black or red in this position on the Σ–D diagram, then this SNR would need to be old, which does not fit. Pavlović et al. (2018) gives an explanation for 1-4 outliers. Alternatively, application of the method from Urošević (2022, 2020) to determine the evolutionary status of newly detected SNRs, the position on the Σ–D diagram (where a single SNR might align with multiple tracks) must relate to the equipartition magnetic field strength and spectral characteristics. According to the literature, MC SNR J0519–6902 is a young SNR, and its position on the Σ–D diagram, equipartition strength, and steep spectrum (–0.62) support this classification. In this paper, the evolutionary phase using Urošević (2022, 2020) is not estimated; instead, assuming it is a young SNR, environmental density is estimated based on the Σ–D tracks.

3.6 Distribution of H I clouds

The distribution of H I in the LMC velocity range towards MC SNR J0519–6902 is shown in Figure 9a where bright H I clouds lie to the south-east. At this radial velocity from ∼220 to ∼270 km s^{-1} alone, H I gas was predominantly present (see Appendix for details). However, we could not confirm an association because the angular resolution of the H I data is roughly twice the diameter of the SNR. The SNR shell H I integrated intensity is ∼600 K km s^{-1}, corresponding to a column density of ∼ 1×10^{21} cm^{-2} under an optically thin assumption (e.g., Dickey & Lockman, 1990).

Figure 9b shows a position–velocity diagram centred near the SNR shell on the edge of an incomplete cavity-like structure of H

---

[i]We use: $\alpha = 0.62$, $\theta = 0.26$ arcmin, $\kappa = 0$, S$_{5.5\,GHz} = 0.045$ Jy, and f = 0.87.
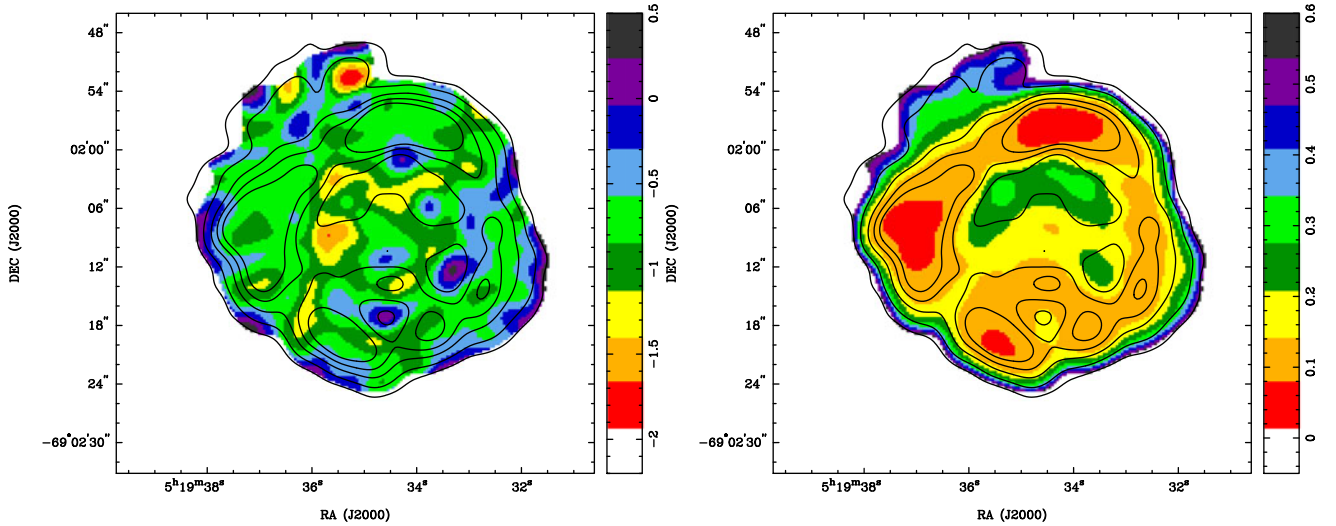
Figure 5. *Left*: Spectral index map of SNR MC SNR J0519–6902 created using 5 500 and 9 000 MHz images. *Right*: Error map of spectral index of SNR MC SNR J0519–6902. Contour lines are overlaid using our ATCA 5 500 MHz image (0.09, 0.2, 0.4, 0.6, and 0.8 mJy beam^{-1}).
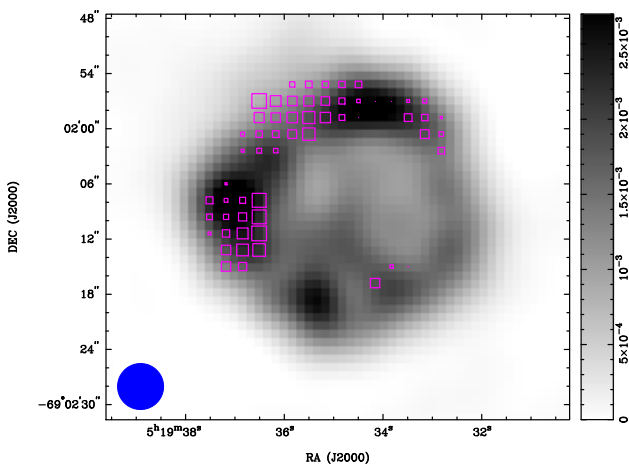

Figure 6. Rotation measure boxes of MC SNR J0519–6902 (ATCA; 4 723, 5 244, 5 756, and 6 268 MHz) overlaid on the ATCA image at 5 500 MHz (greyscale). Most boxes are open (negative values), ranging from a minimum of –314 rad m^{-2} to a maximum of 33 rad m^{-2}. The blue circle in the lower left corner represents a synthesised beam of 5″ × 5″. The bar on the right side represents the greyscale of the 5 500 MHz ATCA image in Jy beam^{-1}.

Figure 7. Magnetic field direction vectors of MC SNR J0519–6902 overlaid on the ATCA image at 5 500 MHz (greyscale). The blue circle in the lower left corner represents a synthesised beam of 5″ × 5″. The bar on the right side represents the greyscale of the 5 500 MHz ATCA image in Jy beam^{-1}.

I that spans a diameter of ∼50 pc and a velocity of ∼30 km s^{-1}, respectively. MC SNR J0519–6902 possibly exploded at the edge of what may be a wind bubble that might have originated from a fast outflow driven from an accreting white dwarf (WD); similar to that proposed for Tycho (Zhou et al., 2016; Tanaka et al., 2021) and N 103B (Sano et al., 2018). Using a model from Leahy (2017) having an updated radius of 3.6 pc in a wind environment, we find new ages with the same model between 250 and 1,100 yrs for various values of the ejecta density profile index (r^{-n} with $n = 6$ to 14), compared to ∼ 2 700 yrs for a uniform circumstellar medium.

At the same time, the tentative bubble may not originate from the progenitor star(s). Those winds eject of order one solar mass
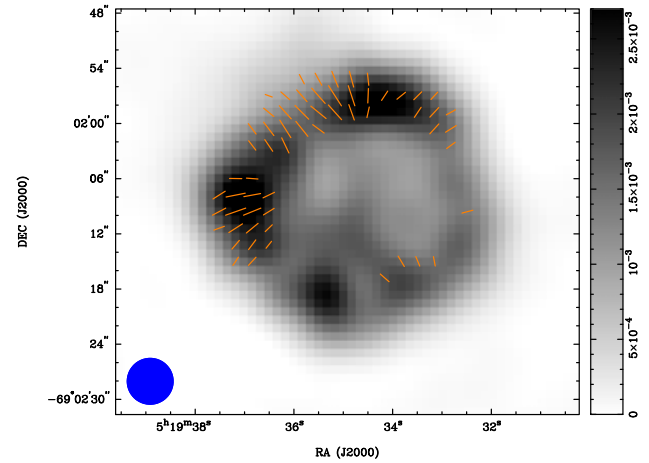
of material at low velocities with low energy. The H I bubble has a size of 30 pc at the distance of the LMC. We use Kwok (2007) to calculate the radius and mass of the swept-up H I shell. Using his Equation (16.62), we obtain the shell radius of 1.9 pc for a wind speed of 20 km s^{-1}, ISM density of 1 cm^{-3} and wind duration of 1 Myrs and 55 pc for a duration of 100 Myrs. The mass of the H I shell would be 0.8 M$_\odot$ and 2×10^4 M$_\odot$ for duration of 1 and 100 Myrs, respectively. The mass of the partial shell feature that is visible in H I in Figure 9b is estimated by integrating the H I over velocity and over the area of the shell (with radius ∼30 pc). The resulting mass in the feature is ∼2.5 M$_\odot$, which is consistent with the theoretical estimate above if the duration of the wind is ∼3 million yrs. The radius of a shell expanding at 10 km s^{-1} for 3 million yrs is 30 pc, consistent with a low-mass stellar wind origin of the shell. In any case, further H I studies with higher
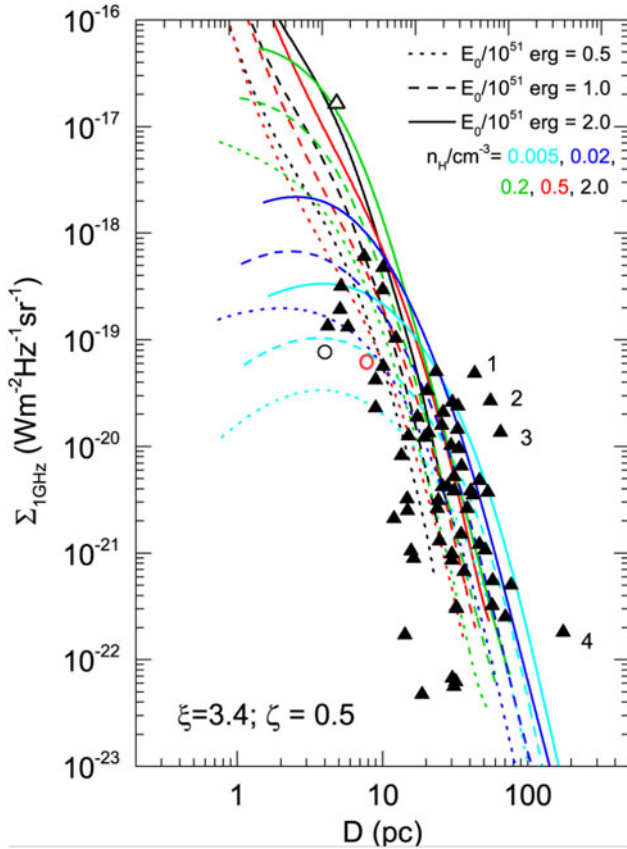
Figure 8. Radio surface brightness–to–diameter diagram for SNRs at a frequency of 1 GHz (black triangles), obtained from numerical simulations (Pavlović et al., 2018, their Figure 3). MC SNR J0519–6902 is marked with an open red circle while the open triangle represents Cassiopeia A. The open black circle represents the youngest Galactic SNR, G1.9+0.3 (Luken et al., 2020). Numbers represent the following SNRs: (1) CTB 37A, (2) Kes 97, (3) CTB 37B, and (4) G65.1+0.6.

angular resolutions are needed to confirm this scenario for MC SNR J0519–6902.

4. Conclusion

We have presented a new radio continuum study of LMC SNR MC SNR J0519–6902. We hypothesise the following:

- MC SNR J0519–6902's polarisation is similar to younger remnants (order 10^2 years) N 103B in the LMC, and, Kepler and G1.9+0.3 in the MW Galaxy. Our remnant has an average fractional polarisation of $5 \pm 1\%$ and $6 \pm 1\%$ at 5 500 and 9 000 MHz, respectively.

- MC SNR J0519–6902 has a spectral index of -0.62 ± 0.02, similar to those of other younger remnants including Kepler and SN 1006.

- We find estimates of the magnetic field strength of this remnant based on our data to be on the order of between 10 and 100 μG, again similar to younger remnants including Kepler and Tycho.

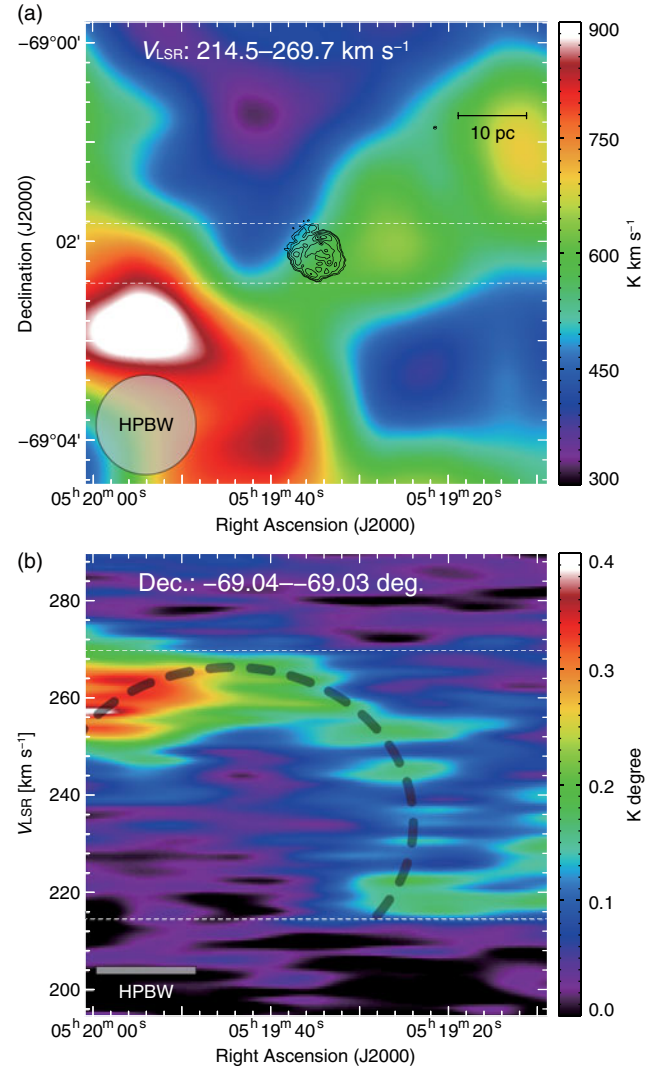- Based on MC SNR J0519–6902's position on our Σ-D track and its age as a young remnant, we suggest it may be

Figure 9. (a) Integrated intensity map of H I towards MC SNR J0519–6902. The integrated velocity range is from 214.5 to 269.7 km s^{-1}. The superposed contours are the same as shown in Figure 1a. (b) Position–velocity diagram of H I. The integrated Declination range is from −69.04° to −69.03°. The dashed curve in the position–velocity diagram indicates the boundary of the H I cavity (see Section 3.6).

at the end of its free expansion phase, entering the Sedov phase of evolution.

- The possible existence of a H I cloud towards the southeast of the remnant and a suspected wind-bubble cavity in this region.

References

Alsaberi, R. Z. E., Barnes, L. A., Filipović, M. D., et al. 2019, Ap&SS, 364, 204

Arbutina, B., Urošević, D., Andjelić, M. M., Pavlović, M. Z., & Vukotić, B. 2012, ApJ, 746, 79

Arbutina, B., Urošević, D., Vučetić, M. M., Pavlović, M. Z., & Vukotić, B. 2013, ApJ, 777, 31

Bozzetto, L. M., Filipović, M. D., Urosevic, D., & Crawford, E. J. 2012, SerAJ, 185, 25

Bozzetto, L. M., Filipović, M. D., Urošević, D., Kothes, R., & Crawford, E. J. 2014, MNRAS, 440, 3220

Bozzetto, L. M., Filipović, M. D., Vukotić, B., et al. 2017, ApJS, 230, 2

Bozzetto, L. M., Filipović, M. D., Sano, H., et al. 2023, MNRAS, 518, 2574

Chu, Y.-H., & Kennicutt, ROBERT C., J. 1988, AJ, 96, 1874

Clarke, J. N., Little, A. G., & Mills, B. Y. 1976, AuJPA, 40, 1

Clarke, T. E. 2004, JKoAS, 37, 337

Collischon, C., Sasaki, M., Mecke, K., Points, S. D., & Klatt, M. A. 2021, A&A, 653, A16

De Horta, A. Y., Filipovic, M. D., Crawford, E. J., et al. 2014, SerAJ, 189, 41

DeLaney, T., Koralesky, B., Rudnick, L., & Dickel, J. R. 2002, ApJ, 580, 914

Desai, K. M., Chu, Y.-H., Gruendl, R. A., et al. 2010, AJ, 140, 584

Dickel, J. R., & Milne, D. K. 1995, AJ, 109, 200

Dickel, J. R., Sault, R., Arendt, R. G., Matsui, Y., & Korista, K. T. 1988, ApJ, 330, 254

Dickey, J. M., & Lockman, F. J. 1990, ARA&A, 28, 215

Edwards, Z. I., Pagnotta, A., & Schaefer, B. E. 2012, ApJ, 747, L19

Filipović, M. D., & Tothill, N. F. H. 2021, c-x-s Principles of Multimessenger Astronomy (IOP Publishing), doi: 10.1088/2514-3433/ac087e

Filipović, M. D., Payne, J. L., Alsaberi, R. Z. E., et al. 2022, MNRAS, 512, 265

Findlay, J. W. 1966, ARA&A, 4, 77

For, B. Q., Staveley-Smith, L., Hurley-Walker, N., et al. 2018, MNRAS, 480, 2743

Fruscione, A., McDowell, J. C., Allen, G. E., et al. 2006, in c-x-s Society of Photo-Optical Instrumentation Engineers (SPIE) Conference Series, Vol. 6270, Society of Photo-Optical Instrumentation Engineers (SPIE) Conference Series, ed. D. R. Silva & R. E. Doxsey, 62701V

Galvin, T. J., & Filipovic, M. D. 2014, SerAJ, 189, 15

Gardner, F. F., & Milne, D. K. 1965, AJ, 70, 754

Gooch, R. 1995, in Astronomical Society of the Pacific Conference Series, Vol. 77, Astronomical Data Analysis Software and Systems IV, ed. R. A. Shaw, H. E. Payne, & J. J. E. Hayes, 144

Hancock, P. J., Trott, C. M., & Hurley-Walker, N. 2018, PASA, 35, e011

Hovey, L., Hughes, J. P., McCully, C., Pandya, V., & Eriksen, K. 2018, ApJ, 862, 148

Kavanagh, P. J., Sasaki, M., Filipović, M. D., et al. 2022, MNRAS, 515, 4099

Kim, S., Staveley-Smith, L., Dopita, M. A., et al. 2003, ApJS, 148, 473

Kosenko, D., Helder, E. A., & Vink, J. 2010, A&A, 519, A11

Kosenko, D., Hillebrandt, W., Kromer, M., et al. 2015, MNRAS, 449, 1441

Kwok, S. 2007, Physics and Chemistry of the Interstellar Medium (Sausalito, Calif, University Science Books)

Leahy, D. A. 2017, ApJ, 837, 36

Li, C.-J., Kerzendorf, W. E., Chu, Y.-H., et al. 2019, ApJ, 886, 99

Long, K. S., Helfand, D. J., & Grabelsky, D. A. 1981, ApJ, 248, 925

Luken, K. J., Filipović, M. D., Maxted, N. I., et al. 2020, MNRAS, 492, 2606

Macri, L. M., Stanek, K. Z., Bersier, D., Greenhill, L. J., & Reid, M. J. 2006, ApJ, 652, 1133

Maggi, P., Haberl, F., Kavanagh, P. J., et al. 2016, A&A, 585, A162

Maggi, P., Filipović, M. D., Vukotić, B., et al. 2019, A&A, 631, A127

Maitra, C., Haberl, F., Maggi, P., et al. 2021, MNRAS, 504, 326

Maitra, C., Haberl, F., Filipović, M. D., et al. 2019, MNRAS, 490, 5494

Mathewson, D. S., Ford, V. L., Dopita, M. A., et al. 1983, ApJS, 51, 345

Mauch, T., Murphy, T., Buttery, H. J., et al. 2003, MNRAS, 342, 1117

Mills, B. Y., Turtle, A. J., Little, A. G., & Durdin, J. M. 1984, AuJPh, 37, 321

Patnaude, D. J., Badenes, C., Park, S., & Laming, J. M. 2012, ApJ, 756, 6

Pavlović, M. Z., Urošević, D., Arbutina, B., et al. 2018, ApJ, 852, 84

Pennock, C. M., van Loon, J. T., Filipović, M. D., et al. 2021, MNRAS, 506, 3540

Pietrzyński, G., Graczyk, D., Gallenne, A., et al. 2019, Nature, 567, 200

Rest, A., Suntzeff, N. B., Olsen, K., et al. 2005, Nature, 438, 1132

Reynolds, S., & Ellison, D. 1992, ApJ, 399, L75

Reynolds, S. P., Gaensler, B. M., & Bocchino, F. 2012, SSRv, 166, 231

Sano, H., Yamane, Y., Tokuda, K., et al. 2018, ApJ, 867, 7

Sault, R. J., Teuben, P. J., & Wright, M. C. H. 1995, in Astronomical Society of the Pacific Conference Series, Vol. 77, Astronomical Data Analysis Software and Systems IV, ed. R. A. Shaw, H. E. Payne, & J. J. E. Hayes, 433

Schenck, A., Park, S., & Post, S. 2016, AJ, 151, 161

Seitenzahl, I. R., Ghavamian, P., Laming, J. M., & Vogt, F. P. A. 2019, PhRvL, 123, 041101

Smith, R. C., Kirshner, R. P., Blair, W. P., & Winkler, P. F. 1991, ApJ, 375, 652

Tanaka, T., Okuno, T., Uchida, H., et al. 2021, ApJ, 906, L3

Tuohy, I. R., Dopita, M. A., Mathewson, D. S., Long, K. S., & Helfand, D. J. 1982, ApJ, 261, 473

Urošević, D. 2020, NatAs, 4, 910

Urošević, D. 2022, PASP, 134, 061001

Urošević, D., Pavlović, M. Z., & Arbutina, B. 2018, ApJ, 855, 59

van der Marel, R. P., & Cioni, M.-R. L. 2001, AJ, 122, 1807

Vukotic, B., Arbutina, B., & Urosevic, D. 2007, RMxAA, 43, 33

Yew, M., Filipović, M. D., Stupar, M., et al. 2021, MNRAS, 500, 2336

Zangrandi, F., Jurk, K., Sasaki, M., et al. 2024, A&A, 692, A237

Zhou, P., Chen, Y., Zhang, Z.-Y., et al. 2016, ApJ, 826, 34

[j]https://atoa.atnf.csiro.au/
[k]https://cxc.cfa.harvard.edu/cda/
[l]https://mast.stsci.edu/portal/Mashup/Clients/Mast/Portal.html

Appendix A. Velocity channel distributions of H I

Figure A1 shows the velocity channel distributions of H I toward MC SNR J0519–6902. We found H I emission only in the velocity range from ∼220 to ∼270 km s^{-1}. Although we could not confirm the cloud association with the SNR due to the modest angular resolution of the H I data, we can infer that the SNR exploded in a relatively low-density gas environment. Further H I observations with high-angular resolution are needed to investigate whether the H I clouds are physically associated with the SNR.
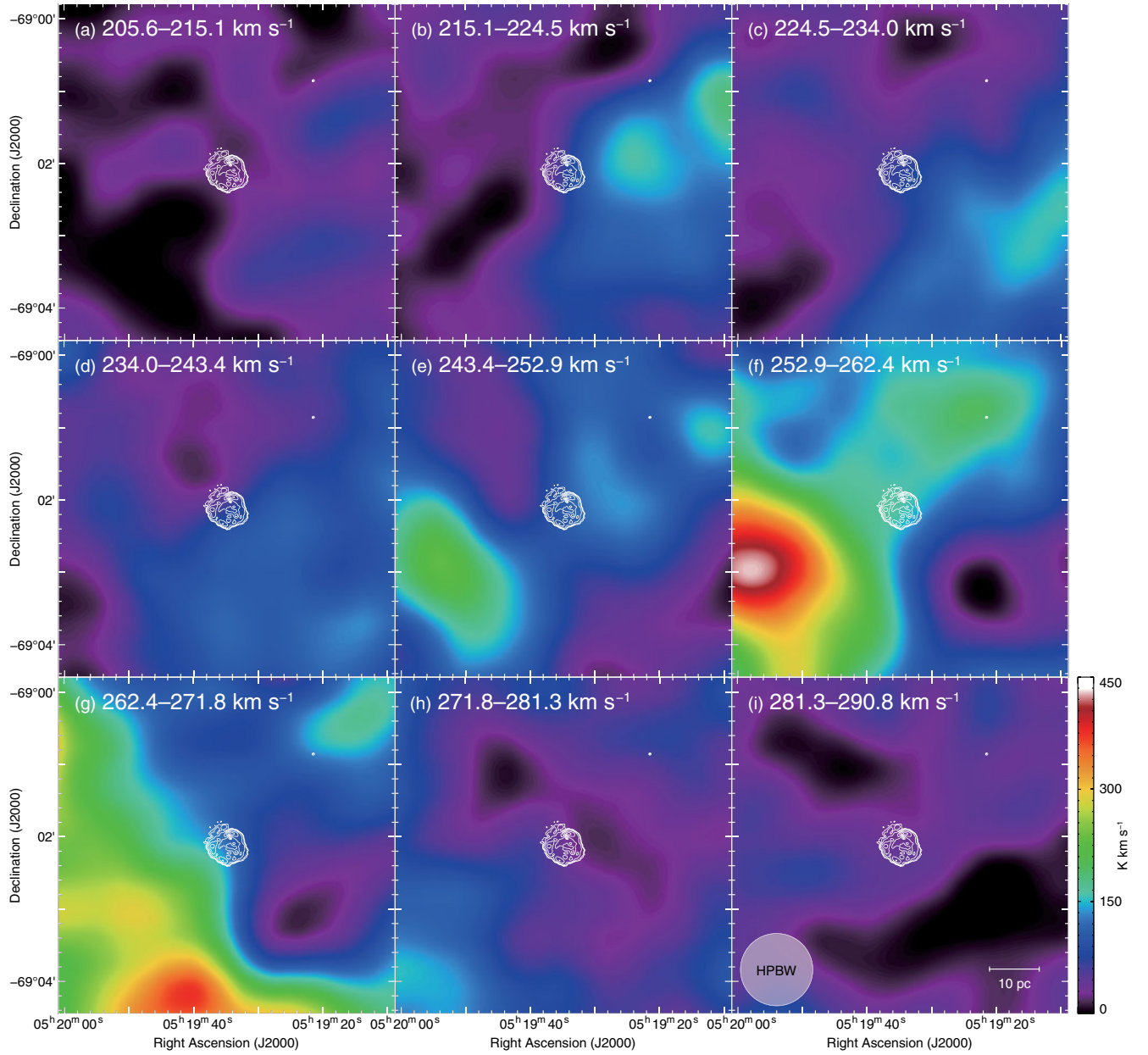
Figure A1. Velocity channel distributions of H I toward MC SNR J0519–6902. The superposed contours are the same as those shown in Figure 1. Each panel shows H I distributions every 9.4 km s^{-1} in a velocity range from 205.6 to 290.8 km s^{-1}.